Aerodynamic investigation of the free flapping flight of a Saker falcon using a 3D multi-view reconstruction method

Martin Heinold*, Christian J. Kähler
Universität der Bundeswehr München, Werner-Heisenberg-Weg-39, 85577 Neubiberg, Germany

ABSTRACT

This paper presents the process of reconstructing a three dimensional point cloud of a Saker falcon's geometry surface from five stereo camera pairs which are mounted on the top, bottom and side of a wind tunnel test section. To obtain three-dimensional point cloud information, corresponding surface point pairs are determined by rectifying camera images and automatically calculating sparse matching features. With the help of a Deep Flow Optical Flow algorithm (DFOF) a dense displacement field is calculated. Specific challenges associated with the 3D reconstruction of a Saker falcon in free flapping flight will be discussed in the paper. Furthermore the flapping flight data of the Saker falcon (*Falco cherrug*) at a mean chord based Reynolds number of about 250,000 will be presented in this paper. An aerodynamic analysis of the free flying falcon, including lift, drag, flight path and angle of attack, will be presented. The analysis shows that the movement of a complete stroke cycle and the structure of the wing surface of the bird can be reconstructed with sufficient accuracy for aerodynamic analysis. This implies that many aerodynamic aspects can be resolved that were not known before. Some examples are offered in the manuscript.

1 INTRODUCTION

The dream of conquering the sky by flying like a bird has been around for many centuries. Most notably Leonardo da Vinci wrote a manuscript in 1505 titled "Codex on the Flight of Birds" in which he details his observations of birds as well as plans and drawings of aircraft. Even though his flight tests failed due to insufficient muscle power, they have laid the foundation for following researchers like Otto Lilienthal or the brothers Wright and continuous research to this day. It is for this reason that Leonardo da Vinci is usually called founder of bionics, the link of biology and technology. Significant aims of the research is to improve the efficiency and optimize the aerodynamic design by learning from a biological model. However, it must be stated that the general believe that the biological selection process leads to optimal designs is wrong for a number of reasons. First, evolutionary processes are always based on specific materials, that must not be optimal for the task. Second, once a structure has evolved for any reason it is not possible to get rid of it in case it limits the performance. Therefore, third the evolutionary process leads most often to locally optimized structures but not to globally optimized designs. In view of flying animals we know birds, insects, bats, fish, flying foxes and ancient flyers. All can fly but non can be considered as a perfect flyer. Fourth, it is not possible to optimize quantities at the same time, that depend on more than one parameter i a non trivial manner. The flapping flight of birds is a reasonable propulsion method at Reynolds numbers about 250000. In a fluid with constant viscosity μ, these Reynolds numbers occur according to $Re = \rho \cdot u \cdot l/\mu$ when the length of the flight object l (which is often the chord of the wing) is sufficiently small or the flight speed u or rather the density of the fluid ρ is low enough. During a flapping cycle the bird wing carries out a strong deformation of the wings surface, which affects the aerodynamics.

To relate the flapping flight motion of the bird with the lift $L = \rho b u \Gamma$ and drag D the deformation of the wing needs to be determined with a contactless measurement method. This technology is able to resolve the flapping motion of the wing over a complete flapping period to measure the wing surface area, the wing span b and the continuous variation of the angle of attacks to determine the circulation Γ. Within the scope of a joint research project (DFG-SPP1207) Bachmann and Wagner [1], Friedl and Kähler [2] and Wolf and Konrath [3] investigated the gliding flight of barn owls (*Tyto alba*). The researchers evaluated and compared different experimental methods setups. Stationary and moving camera systems were examined. Moving imaging systems have shown advantages during the evaluation process of the data because the bird needs more time to pass the observation field, which allows for the capturing of more than one flapping cycle. On the other hand the background separation is rather complicated because the background is moving. Furthermore a moving camera frame can irritate the bird and leads to unnatural behavior. Stationary cameras simplify the masking of a moving object from a fixed background. Other 3D-measurement tech-

*Email address(es): martin.heinold@unibw.de

niques like Time-of-Flight cameras [4] allow for calculating distances by measuring light travel time. However usage of more than one system or background light can lead to disturbances with uncertainties of mm up to cm. Ponitz et.al. [5] recorded peregrine falcon (*Falco peregrinus*) during dive experiments along a dam wall. The trajectory of the falcon was calculated with the help of stereo reconstruction of a single marked point on the bird. Three more cameras took images of the falcon from different perspectives to understand the motion and the shape of the bird. Thereby it was possible to explain the diving flight, but the wings fit closely to the body during that maneuver to reduce drag. Only for the change of direction the wing was folded out. The flapping motion was studied by Carruthers et.al. [6] with six cameras and a Steppe Eagle (*Aquila nipalensis*). The research showed that the leading edge of the bird is important for the aerodynamic analysis. The relatively low recording rate of $25\,\mathrm{fps}$ demonstrates problems with a complex and fast motion like the flapping flight. In that case a flapping cycle lasts about $0.2 - 0.25\,\mathrm{s}$ and only $4 - 6$ images resolve the whole motion. Positions like the upper and lower dead center need to be precisely resolved over time because the curvature, the angle of attack and the wing shape change significantly. Additionally surface points were chosen by manually clicking 390 correspondence points and reconstruct these. The precision and the reproducibility seem to complicated. Therefore a system was developed that is able to automatically reconstruct the wing surface of a flapping bird with a sufficient recording rate. To obtain 3D point clouds from multiple camera images our method uses procedures from Computer Vision. After a volumetric calibration (mathematical relation between 2D image coordinates (x, y) and 3D real world coordinates (X, Y, Z)), correspondences between two or more cameras are obtained by automatic calculation of sparse feature points. With the help of a DFOF algorithm a dense disparity map is determined and triangulated to get 3D coordinates. Aerodynamic characteristics, like angle of attack variations, wing half span s, the flapping frequency f_{falcon} the falcon speed u_{falcon} as well as lift L are presented in this paper.

2 MEASUREMENT SETUP

The atmospheric wind tunnel of the Bundeswehr University Munich was used for the measurements of flapping flight of a Saker falcon (*Falco cherrug*). Two birds, a male ($720\,\mathrm{g}$, wingspan about $1\,\mathrm{m}$) and a female ($1040\,\mathrm{g}$, wingspan about $1.1\,\mathrm{m}$) were trained to fly through the wind tunnel against a uniform flow with velocities from $10\,\mathrm{m/s}$ to $18\,\mathrm{m/s}$. As a result of the headwind, the time of flight in the measuring area increases and more than one flapping period can be recorded to make a statistical analysis of the whole flapping cycle possible. The test section of the open loop wind tunnel has a cross-section of $1.85\,\mathrm{m} \times 1.85\,\mathrm{m}$ and measures $22\,\mathrm{m}$ in length. The facility can produce velocities between $2\,\mathrm{m/s}$ and $45\,\mathrm{m/s}$. The turbulence level in the test section was measured

Figure 1: Male Saker falcon with natural pronounced texture on the upper and lower body

Tu $= \sqrt{\overline{u'^2}}/u_\infty = 0.5\%$. That imitates real world conditions in the lower atmosphere near the ground. The data was acquired simultaneously with 10 pco.dimax highspeed cameras from PCO. The camera sensor of these cameras generates full frame images with $2016\,\mathrm{px} \times 2016\,\mathrm{px}$ resolution, recorded with $1279\,\mathrm{fps}$. To resolve the motion of a wing up- and downstroke over time precisely, a frame rate for the recordings of $1000\,\mathrm{fps}$ was sufficient. The highspeed cameras with baselines of $800 - 1200\,\mathrm{mm}$ were equipped with Zeiss Distagon $35\,\mathrm{mm}$ lenses (f-number of 11) with a working distance between camera and measurement object of approximately $1\,\mathrm{m}$.

3 CAMERA CALIBRATION

To reconstruct a 3D point cloud with more than two cameras into the identical reference coordinate a camera pinhole model is reasonable. The camera matrices $\mathbf{P}_i$ of every camera consist of intrinsic ($\mathbf{A}$) and extrinsic parameters ($\mathbf{K}$). $\mathbf{A}$ contains the focal length of the objective, the physical size of each pixel on the camera sensor s (s_{x} and s_{y} for non-square pixels) and the principal point u_0 and v_0. To obtain the mathematical conversion from the three dimensional world coordinates $\mathbf{X} = (X, Y, Z)^{\mathrm{T}}$ to sensor coordinates $\mathbf{x} = (x, y)^{\mathrm{T}}$ and the relative rotation $\mathbf{R}$ by Euler angles and translation $\mathbf{t}$ of the camera, marked points on a two plane calibration target are detected (see Figure 2). The calibration pattern is moved rotatory and translational through the measurement domain. The reference coordinate system is setup at the first position of the pattern where the $X - Y$-plane is plane-parallel to the target and the Z-axis is perpendicular to it. To align the world coordinate system with the wind tunnel walls three reference points each on the top and bottom of the channel allow for transforming the coordinate system so that the X-axis is parallel to the streamwise direction. Z is from the bottom to the

Figure 2: Two plane calibration target (LaVision type 31): point to point distance 15 mm, point diameter 3 mm, plane height 3 mm, plate thickness 14.8 mm [7]

top of the wind tunnel and Y is perpendicular to X and Z.

To transform a point from a 3D space onto the 2D camera coordinate system successive multiplication and addition is required. The reduction of complexity is achieved by using homogeneous coordinates. As a result the transformation is applied as a matrix multiplication.

$$\begin{aligned}\begin{pmatrix} x^* \\ y^* \\ 1 \end{pmatrix} &= \mathbf{K} \cdot \begin{pmatrix} X \\ Y \\ Z \\ 1 \end{pmatrix} \\ &= \left[R_\mathrm{z} \cdot R_\mathrm{y} \cdot R_\mathrm{x} | \begin{pmatrix} t_\mathrm{x} \\ t_\mathrm{y} \\ t_\mathrm{z} \end{pmatrix} \right] \cdot \begin{pmatrix} X \\ Y \\ Z \\ 1 \end{pmatrix}\end{aligned} \tag{1}$$

$$\begin{aligned}\begin{pmatrix} x \\ y \\ 1 \end{pmatrix} &= \mathbf{A} \cdot \begin{pmatrix} x^* \\ y^* \\ 1 \end{pmatrix} \\ &= \begin{bmatrix} \frac{f}{s} & 0 & u_0 \\ 0 & \frac{-f}{s} & -v_0 + h \\ 0 & 0 & 1 \end{bmatrix} \cdot \begin{pmatrix} x^* \\ y^* \\ 1 \end{pmatrix}\end{aligned} \tag{2}$$

Distortion on the basis of lens curvature, like radial and barrel distortion, affect the pinhole assumption of straight lines between 3D world points and the camera center. By calculating the undistorted pixel coordinates with the distortion coefficients this bias can be corrected. Due to the production quality of the Zeiss lenses distortions play only a minor role, despite everything high order polynomials correct the distorted pixel coordinates [8]. Basis for the stereo reconstruction is the projective geometry between two cameras. Corresponding point pairs $\mathbf{x} = (x, y)$ and $\mathbf{x}' = (x', y')$ from the calibration pattern comply with the fundamental equation.

$$\mathbf{x}'^T \cdot \mathbf{F} \cdot \mathbf{x} = 0 \tag{3}$$

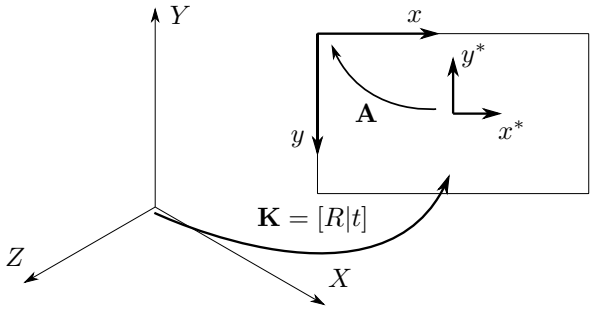

Figure 3: Translation t and rotation R of the world coordinate system ((X, Y, Z) in m) on to the camera sensor center ((x^*, y^*) in m). Afterwards recalculation of the camera coordinate system into px units ((x, y) in px)

$\mathbf{x}'^T \cdot \mathbf{F}$ and $\mathbf{F} \cdot \mathbf{x}$ describe respectively projected lines from one point $\mathbf{x}'$ or $\mathbf{x}$ to a line $\mathbf{l}'$ or l on the other camera sensor in each case. All lines intersect in one point, the epipole. To reduce the complexity of the correspondence search, the epipoles on both sensors are mapped to infinity by means of $\mathbf{T}_1$ and $\mathbf{T}_2$ [9]. This process is called rectification and is displayed In Figure 4. Lines, intersecting only at infinity, need to be horizontal. Hence the correspondence point search reduces to a one dimensional problem along the epipolar lines.

4 DENSE DISPARITY MAP CALCULATION

The shift between one characteristic point in two images along the epipolar line is called disparity (see Figure 4). The displacement is inversely proportional to the depth of a point. In principle only the length of the baseline and the focal lengths of the cameras, both information from the camera calibration, are required to calculate the depth of a 3D world point as shown in equation (4) [10].

$$d = x - x' = \frac{Bf}{Z} \tag{4}$$

The determination of corresponding point pairs in camera setups with huge baselines leads to ambiguities and occlusions. To reduce the analysis effort of calculating dense displacement maps the first step is to detect sparse corresponding features.

The relevant part of the image, the flapping falcon, is segmented from the resting background by subtracting the images, preprocessed with a canny edge filter, and carry out a logical xor operation. Remaining noise can be removed with an area opening. Parts of the bird that overlap with edges from the background need to be filled by an erosion and a morphological fill function. The masks can be temporally smoothed with the help of Optical Flow. Five consecutive time steps are back projected to the initial time step and a median filter is applied (see Figure 5).

Brox et.al. [11] proposed a formulation of Optical flow that minimizes the energy function in equation (5)

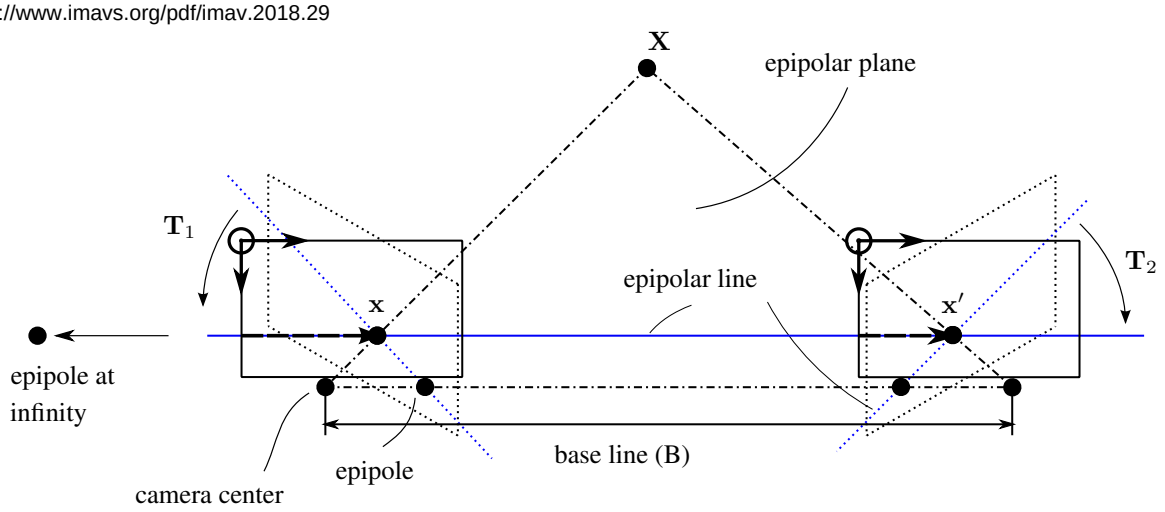

Figure 4: Rectification by means of epipolar geometry: a 3D world point $\mathbf{X}$ is displayed on two camera sensors at the points $\mathbf{x}$ and $\mathbf{x}'$. Epipoles calculated with the help of corresponding calibration points are mapped to infinity by multiplication of transformation matrices $\mathbf{T}_1$ and $\mathbf{T}_2$

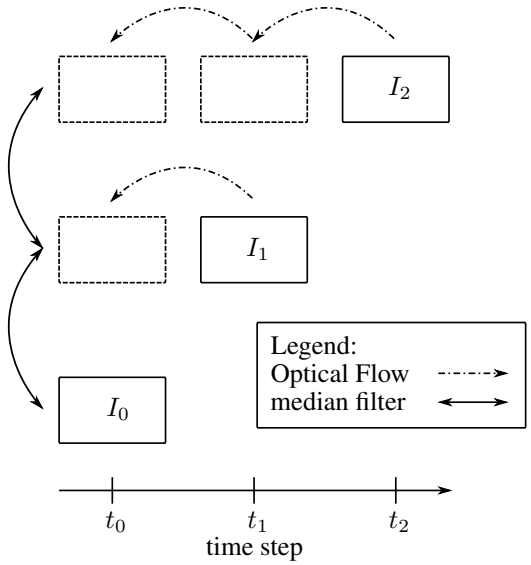

Figure 5: Schematically presentation of temporal smoothing with 3 time steps

$$
\begin{aligned}
E(\mathbf{w}) = &\int_\Omega \Psi(|I(\mathbf{x}+\mathbf{w}) - I(\mathbf{x})|^2)\mathrm{d}\mathbf{x} \\
&+ \gamma \int_\Omega \Psi(|\nabla I(\mathbf{x}+\mathbf{w}) - \nabla I(\mathbf{x})|^2)\mathrm{d}\mathbf{x} \\
&+ \alpha \int_\Omega \Psi(|\nabla u|^2 + |\nabla v|^2)\mathrm{d}\mathbf{x}
\end{aligned} \tag{5}
$$

with the following comments:

$$\mathbf{w} = (u, v, 1)^{\mathrm{T}} \tag{6}$$

$$\Psi(s^2) = \sqrt{s^2 + \epsilon^2} \text{ with } \epsilon = 0.001 \tag{7}$$

The robust expression with the help of l_2 or Euclidean norm is presented in equation (7). Equation (5) contains a constant intensity term, a constant gradient term along edges and a velocity field smoothness term. The parameters for regularization α, the weight γ and the scaling factor of the Gaussian pyramid were determined by Heinold and Kähler [12].

In Figure 6 the falcon image and the resulting mask is shown. On the leading edge of the right wing a streak is visible that over segments the falcon. Due to different lighting situations during calibration and the recording, areas in the background can get a higher weight during edge detection and remain in the image after segmentation. On the basis of the stripe that is connected to the birds mask, the area open method does not remove this part. To avoid losing information from the wing, over segmentation is preferred compared to under segmentation where areas of the bird are missing.

Only within the masks corresponding points are searched to reduce the computational expense. Furthermore a wing flap consist of about 250 to 300 images but only every 10th

Figure 6: Foreground / Background segmentation of a Saker falcon by background subtraction: left image – rectified falcon image from top view, right image – mask of the falcon

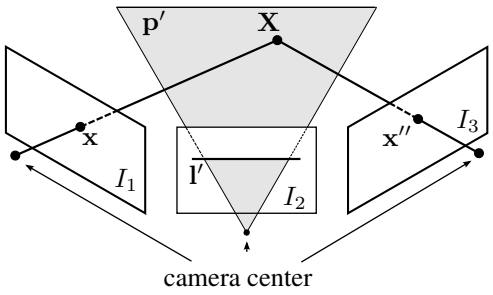

Figure 7: Transfer from one point $\mathbf{x}$ via plane $\mathbf{p}'$ to point $\mathbf{x}''$ (following [19, p. 382])

images is used to detect sparse feature points. To reduce noise and enhance high frequency signals in the image, at first the stereo images are subtracted of the sliding minimum (window size $9\,\mathrm{px} \times 9\,\mathrm{px}$). Possible prominent features are corners, that can be located with a minimum eigenvalue algorithm [13]. All corner points in one camera are normalized cross correlated with stripes of the second camera image on the same epipolar line [14]. Four different window size ($12\,\mathrm{px} \times 12\,\mathrm{px}$, $24\,\mathrm{px} \times 24\,\mathrm{px}$, $48\,\mathrm{px} \times 48\,\mathrm{px}$ and $64\,\mathrm{px} \times 64\,\mathrm{px}$) are used to detect feature in various sizes. Only correlation maxima higher than 1.5 times the correlation value of the second highest peak are considered matches [15]. To locate the position with subpixel accuracy a gaussian fit is implemented. The process is repeated with corners from the second camera and stripes in the first camera image. To increase the number of matches an improved SIFT-algorithm is applied [16, 17, 18]. The corresponding point pairs are searched for outliers by using a RANSAC algorithm for a homography [19].

With the help of Optical Flow the matching point pairs are distributed back and forth in the timeseries (see Figure 9). To prevent matches to be wrong, point pairs from one time step to another are cross correlated. The shift between two time steps is significantly lower than between two different, rectified cameras. Therefore the selection process of matches simplifies to choosing matches with normalized correlation values higher than 0.8.

To increase the amount of point correspondences more than two cameras can be used. With the help of a Trifocal tensor T_f it is possible to perform a point transformation from two cameras to a third one [19] (see Figure 7). In Figure 8 it is shown that every two cameras from a set of cameras with overlapping point of view can transfer corresponding points $\mathbf{x}$ and $\mathbf{x}'$ to a third camera $\mathbf{x}''$. To calculate the coordinate in the third view a line $\mathbf{l}'$ is selected that passes through $\mathbf{x}'$ and spans a plane $\mathbf{p}'$. With that the position $\mathbf{x}''$ is determined in tensor notation (compare [19, p. 376]) by:

$$x''^k = x^i l'_j T_i^{jk} \tag{8}$$

The search for corresponding point pairs can be parallelized because the individual calculations every 10th time step are independent from each other. Therefore the distribution to more workers reduces the evaluation time about the factor of the number of workers. The small difference occurs by virtue of more data copying processes there and back to every single worker. During the analysis a PC with an Intel Core i7-4930K processor (6 cores with $3.4\,\mathrm{GHz}$ each), $32\,\mathrm{GB}$ RAM and a Nvidia GeForce GTX 660 (960 Shaders, $993\,\mathrm{MHz}$ GPU Clock, $2\,\mathrm{GB}$ RAM) was used. The evaluation was done with MATLAB R2017a and OpenCV 3.2.0.

The evaluation showed that two different formulations of

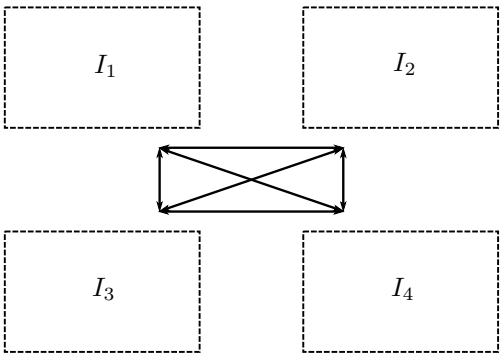

Figure 8: For every set of three cameras with overlapping point of view a Trifocal tensor can be set up

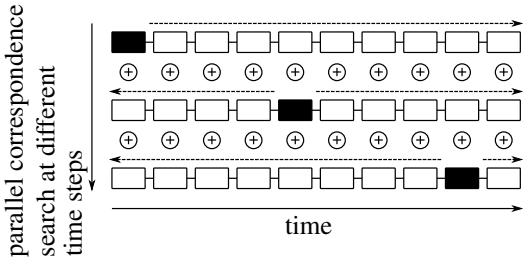

Figure 9: Diagram of the parallel search for corresponding points and spread out with Optical flow (dotted arrow) to time steps before and after, schematically depicted for every 4th time step (black box). Finally summation of all correspondences for one time step

Figure 10: Left image: spatial smoothed disparity map, right image: spatial and temporally smoothed disparity map – gray values from dark gray to white indicate higher disparity and lower depth value – mask is applied to the picture (black background)

the Optical Flow are necessary for the computation of a dense disparity field. For image sequences with small shifts between consecutive images equation (5) from Brox et.al. [11] shows strong results. On the other hand an extension of the formulation is required for the computation of correspondences between different cameras. With the input of sparse corresponding point pairs a Deep Flow Optical Flow algorithm is able to calculate a dense disparity map [20].

$$E(\mathbf{w}) = \int_\Omega E_{\text{Data}} \mathrm{d}\mathbf{x} + \alpha \int_\Omega E_{\text{Smoothnes}} \mathrm{d}\mathbf{x} + \chi \int_\Omega E_{\text{Matching}} \mathrm{d}\mathbf{x} \tag{9}$$

The third term in equation (9) includes information of the sparse correspondences. Furthermore the variable χ determines the weight of the sparse matches as shown in Stoll et.al. [21].

The Deep Flow algorithm spatially smooths the disparity map. To close holes in the displacement field and remove outlier disparities a temporal smoothing method, as explained on page 3, is applied to the disparity map.

5 TRIANGULATION OF THE POINTCLOUD

Every value in the disparity map represents a displacement from one image to another. These corresponding points can be triangulated into 3D space with the help of the camera matrices $\mathbf{P}_i$ and the fundamental matrix $\mathbf{F}$. Using the optimal triangulation method proposed in [19], three dimensional coordinates (X, Y, Z) are calculated and thereby the sum of squared distances is minimized in accordance to the fundamental equation (3).

To reduce the amount of remaining outliers to consecutive steps are used. At first the triangulated world points $\mathbf{X}$ are back projected on the left camera sensor $\hat{\mathbf{x}}$.

$$\hat{\mathbf{x}} = \mathbf{P}_1 \cdot \mathbf{X} \tag{10}$$

Only points which are located inside the left image mask are kept. The second step outliers are detected by Sparse Outlier Removal algorithm [22]. The foundation of the program

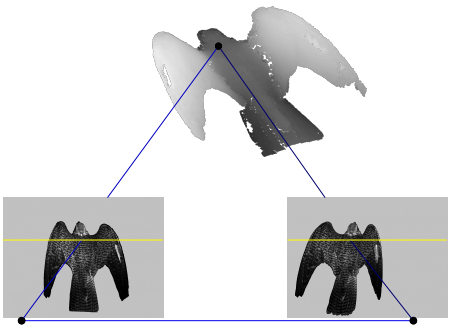

Figure 11: 3D point cloud reconstruction

is a nearest neighbor search around every point within a specified amount of points (during the evaluation 200 was chosen). The point distribution is examined and points outside a certain allocation are removed.

6 UNCERTAINTY ANALYSIS

It is difficult to define an uncertainty for a stereo reconstruction algorithm. One of the most used kind of uncertainty is the re-projection error [23]. To determine the error there is a similar approach like in section 5. The world coordinates are back projected on the camera sensor by multiplying the camera matrices $\mathbf{P}_i$ onto the 3D point (see equation (10)). With the resulting n point positions $\hat{\mathbf{x}}$ and $\hat{\mathbf{x}}'$ the geometrical distance to the original points $\mathbf{x}$ and $\mathbf{x}'$ is calculated.

$$\text{Err} = \sum_i^n d(\mathbf{x}_i, \hat{\mathbf{x}}_i)^2 + d(\mathbf{x}'_i, \hat{\mathbf{x}}'_i)^2 \tag{11}$$

During the analysis an error Err of $0.3965\,\text{px}$ was measured.

To make further statements about the uncertainty in an experimental setup prior to the measurement campaign with the Saker falcon a well-defined plate with a random dot pattern on it was moved by a traversing unit. The plate had a thickness of $8\,\text{mm}$ and it was moved along the Z-axis of the coordinate system through the measurement domain in $25\,\text{mm}$ steps.

The plate was reconstructed for 9 consecutive steps and the mean displacement between the moves is $24.48\,\text{mm}$. The mean relative difference to the real movement is therefore calculated to $0.52\,\text{mm}$. Two cameras reconstructed the upper side of the plate and two cameras the lower side. Hence the thickness of the aluminum plate was calculated and the absolute mean deviation was $0.19\,\text{mm}$ from the real size.

7 AERODYNAMIC ANALYSIS

During the measurement campaign over 50 flights of two falcons (one female, one male) in the Atmospheric Windtunnel Munich at different incoming flow velocities were performed. This paper focuses on one flight of the female Saker falcon at $u_\infty = 18\,\text{m/s}$ wind speed. During the flight through

Figure 12: Well-define aluminum plate with random dot pattern, thickness 8 mm – moved by traversing unit along Z-axis in 25 mm steps

730 time steps were recorded and are evaluated for the analysis. The coordinate system is an aerodynamic coordinate system with the following orientation: X is in the inflow direction, Y along the wingspan of the right wing and Z depicts the height. The subscript $b, t = 0$ means a fixation of the coordinate system in the first time step of the evaluation at a prominent point of the back of the bird ($X_{\mathrm{b,t=0}}, Y_{\mathrm{b,t=0}}, Z_{\mathrm{b,t=0}}$). Furthermore to simplify the discussion a non-dimensional coordinate along the Y-axis is defined by dividing the Y-position with the current half-span s in every time step. To compare different flaps with each other a phase angle is introduced. $0°$ is the highest body position, $180°$ the lowest one (compare Figure 13).

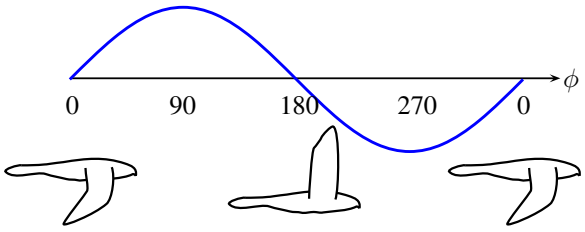

Figure 13: Definition of phase angle ϕ.

$$\zeta(Y, \phi) = \frac{Y(\phi)}{s(\phi)} \tag{12}$$

Figure 14 shows the variation of the wing half-span over the phase angle. During the up- and downstroke of the third flap the outermost feathers of the wing are out of the image. Additionally the lighting of the hand wing is faint. Therefore the local maximum of the half span is underestimated in comparison to the first two flaps which were almost perfectly

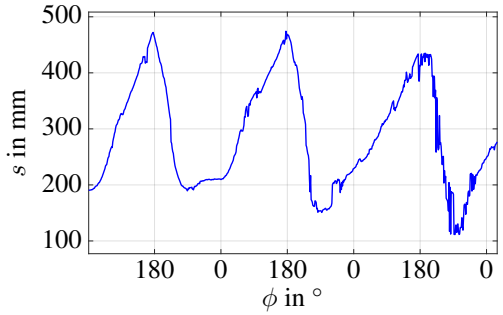

Figure 14: Maximum wing half span $s_{\max}$ plotted over phase angle ϕ.

recorded. The analysis of the first two flapping cycles shows the high reproducibility of the flapping. This demonstrates the abilities of the falcon and our developed measurement technique. Read from Figure 14 the global wing half span is equal to $s_{\max} = 474\,\mathrm{mm}$.

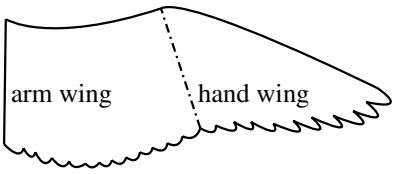

(a)

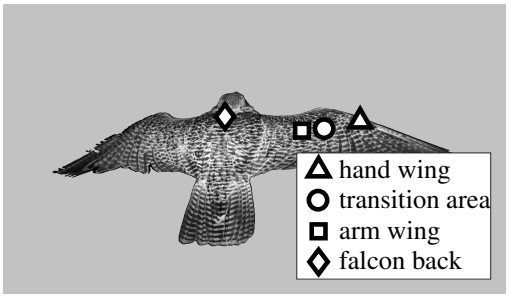

(b)

Figure 15: (a): Diagram of a bird's wing (following [24, p. 30]), (b): Points viewed on the wing (arm wing – square, hand wing – triangle, transitional area – circle) and back of the bird (diamond).

The analysis of the bird aerodynamics can be quantitatively done by looking at the flight patch of the falcon. In Figure 15 four specific points on the top of the bird are regarded. One point in the middle of the falcon body and three different positions on the right wing. These are divided into one point on the arm wing ($\zeta = 0.308$), one on the hand wing ($\zeta = 0.539$) and the last one in the transitional area

($\zeta = 0.397$). In Figure 15 (a) a schematic representation of a falcon wing is shown. From this image it is recognizable that the structure of the wing allows for the variation of the leading edge bearing ψ during a flapping cycle. The selection of a point on the arm wing and one on the hand wing is relevant on the basis of two completely different angles ψ with regard to the Y axis. This characteristic produces various motions on the different wing positions what leads to different aerodynamic performance.

During a flapping cycle the wing lifts up followed by a downstroke. To understand the differences of a falcon flap in comparison to a fixed flapping wing the relative differences between the three wing positions and the movement of the body is shown in Figure 18. In Z direction all three points on the wing follow a sinusoidal motion and the amplitude increases towards further outlying wing positions (see Figure 18 (c)). This behavior would be similar to the mentioned fixed flapping wing. In Figure 18 (a) and Figure 18 (b) the large displacement of the hand wing and the relative small movement of the arm wing are presented. Figure 18 (b) shows a similar course of all three curves. Only in the range of extrema ($\phi \approx 190°$) does the amplitude increase significantly in the span direction. This can be explained above all by the high dynamics of the arm wing. For clarity the motion is depicted from at four different phase angles from a top view camera in Figure 17.

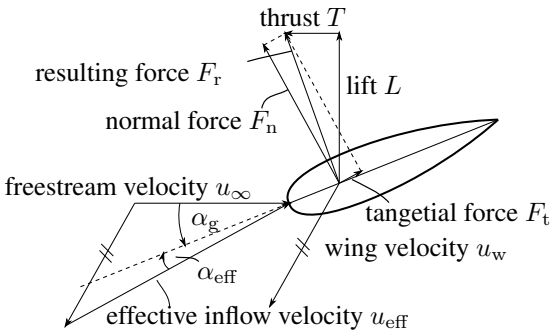

Figure 16: Lift and thrust generation of a moving wing on the basis of different angles of attack. Geometrical AOA α_g for a steady wing. For analysis, the wing is approached at the effective AOA α_eff. [25]

In Figure 19 the motion of the point on the back of the bird is depicted over the phase angle ϕ. Because a 3D representation is to complicated the three-dimensional flight path is shown in three different lines of sight ($X-\phi, Y-\phi, Z-\phi$). The movement in Figure $Z-\phi$ presents a sinusoidal form and a downward gliding motion. To conserve angular momentum the natural reaction to compensate the wing motion is the up and down movement of the body. As a result the maximum position of the bird body corresponds nearly to the local minimum of the wing and vice versa. During a upstroke of the wing the body is lowered and the other way around. There is a small lag of the wing motion in comparison to the body. The downward movement during the first flapping cycle can be explained by the fact that the falcon must first determine its target after the start and then moves to the corresponding position and height. The Figure $Y - \phi$ shows that the falcon does not fly precisely against the incoming flow direction. This observation can be explained by the target of the falcon. To start a flight the bird is attracted by a falconer with some food (a common quail or a parts of a rat). As a predator the falcon focuses on the object and changes the flight path during the measurement to the right and downwards. Due to the high steady incoming flow velocity the flight distance in X direction is small. In nature without wind influence the real flight distance would be the measured distance divided by the falcon speed $u_\mathrm{falcon} = 1.36\,\mathrm{m/s}$ and multiplied with the total velocity $u_\mathrm{total} = u_\mathrm{falcon} + u_\infty = 19.36\,\mathrm{m/s}$. In this case the bird would have traveled roughly $13.5\,\mathrm{m}$ during the measurement. Combined with the downward motion in Z-direction during the flapping cycles the gliding angle is determined by equation (13).

$$\gamma = \frac{\Delta Z}{\Delta X_\mathrm{total}} = -0.887° \tag{13}$$

In addition, the flapping frequency is determined with the aid of Figure 20 (a). For this purpose the highest local peaks of the periodic motion are detected to determine the frequency of $f_\mathrm{falcon} = 4.35\,\mathrm{Hz}$.

Figure 20 shows the movement of the prominent wing positions. Close to the falcon body the curve is smooth and monotonous. Rapid changes in the direction of movement on the arm wing lead to complex curves (see Figure 20 (c) and (b) at approximately $\phi \approx 0°$). Due to manoeuvring (slight right turn and descent), there is no complete symmetry between the wing flap (compare Figure 20 (c) arm wing motion at $\phi \approx 270°$).

$$L = c_\mathrm{L} \cdot \rho/2 \cdot u_\mathrm{total}^2 \cdot S \tag{14}$$

For a detailed aerodynamic evaluation the consideration of the wing profiles during the flapping cycle is necessary. Therefore, in the following section the wing cross-section at $\zeta = 0.55$ is examined. The wing profiles shown are taken from the second flapping cycle. In Figure 17 the pictures (a) to (d) show an upstroke of the wing, over the turning point and a downstroke (the highest point is reached at phase angle $\phi = 120°$). The evaluation of the profiles is limited to 70% of the total stroke due to the increasing uncertainty near the lower turning point as well as occlusions of the wing. The influence of aerodynamics on the bird is rather marginal at this time, since no lift is generated. Based on equation (14), the lift force is linked to the wing area. As this becomes minimal near the lower turning point, there is also only a minimal lift at this point. The airfoil cross-sections in Figure 21 are taken in a period of time between the pictures 17 (b) and (d).

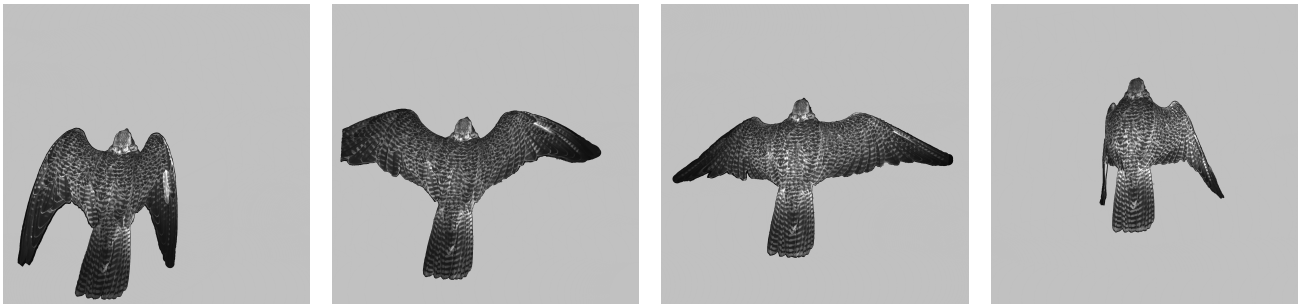

(a) (b) (c) (d)

Figure 17: Snapshots from the flapping cycle of a Saker falcon ($\Delta t = 50\,\mathrm{ms}$). [25]

Based on these geometries Xfoil simulations were performed to estimate the aerodynamic properties of the profiles [26]. The free stream turbulence intensity of the Atmospheric Windtunnel Munich was measured to $Tu = 0.5\,\%$ at the used inflow velocities by Herbst et.al. [27]. To forecast the transition of 2D boundary layers in incompressible flows with the help of linear stability theory Van Ingen [28] developed the e^N method. Xfoil uses this method and calculates the N factor as shown in the following equation:

$$N = -8.43 - 2.4 \cdot \ln\left(\frac{Tu}{100\,\%}\right) \tag{15}$$

For further examination N is calculated as 4.2. It should be noted that the surface roughness of birds is higher than that of modern aircraft wings (compare Reichardt [29]). For this reason, lower N values of up to 1 would be possible to take the influence of surface roughness into account [26]. However, here we are interested in the sensitivity of aerodynamic performance to support aerodynamic analysis rather than absolute values.

The analysis of thickness and camber enables the calculation of geometric parameters. Figures 22 and 23 show positions and aerodynamic values of the profile in relation to thickness and curvature. In this phase of the stroke cycle, the position of the maximum thickness moves relative to the leading edge and the maximum thickness itself decreases significantly by about 50% before a further increase becomes apparent. Before phase angle $175°$ the average position X_{th}/c is 0.28. After the upper turning point, a position of about 0.14 is set. Based on the potential theory, the thickness distribution is responsible for the speed around the profile. An earlier position of the maximum thickness th/c indicates a greater curvature of the profile at the leading edge and thus a higher acceleration.

The maximum curvature f/c varies only slightly over the phase angle. However, the position of the maximum curvature X_{f}/c seems to move further back to the trailing edge until the upstroke becomes a downstroke. Then the value returns to a position of about 0.45.

Figure 24 shows the change in attack angles α_{g} and α_{eff} during the observed time period. During this stage of the flap, the effective AOA starts at high negative numbers, reaches $0°$ at the upper turning point and then rises further. These findings can be explained by the complex motion of the falcon. During a flapping cycle, not only lift has to be generated. The falcon also needs thrust to travel forward. The geometric AOA α_{g} of a constant inflow (negative for the downstroke, about $0°$ at upstroke) must be corrected by the movement of the wing. The effective AOA α_{eff} is shown in figure 24 (b). Therefore, a negative geometric angle of attack allows a vectorial decomposition of the attacking forces into lift and a horizontal part, thrust, as shown in figure 16. Even if the geometry of the profile changes during the stroke cycle, Figure 25 (b) shows a linear slope between $\alpha = -8°$ and $10°$ and the lift coefficient c_{l}. This allows to calculate a zero lift angle (α_0) of about $-3.2°$ and a lift coefficient at AOA $0°$ of $c_{\mathrm{l},0} = 0.4$.

The Reynolds number of a fixed wing under constant flow conditions (free flow velocity and viscosity) is calculated only once. Due to the large deformation and motion of the falcon wing, the Reynolds number changes at every phase angle. Nevertheless, the inflow conditions are almost uniform. With the definition of the Reynolds number:

$$Re = \frac{u \cdot c}{\nu} \tag{16}$$

Figure 24 can also be considered a variation of the chord length c. Before phase angle $175°$, the arm wing is near the body. Therefore, the chord length c at a relative position $\zeta = 0.55$ is so high at an upstroke, and rather steady in the process of the downstroke. Pulling up the wing during upstroke reduces drag and the profile generates downforce. As a result, the lift-to-drag coefficient $c_{\mathrm{l}}/c_{\mathrm{d}}$ in Figure 25 is slightly negative during this phase of the flap. The results during the downstroke show the efficiency of the natural propulsion system. Even with large wing motions and a upstroke phase, a lift coefficient of up to 50 can be achieved, which is a considerable value.

8 CONCLUSION

This paper presented a method to reconstruct a point cloud of the natural texture of a real Saker falcon flying in a wind-tunnel from the synchronized recordings of multiple cameras. To calculate the wing surface from both sides over a full flapping cycle 10 highspeed cameras were installed around the test-section of an atmospheric wind tunnel and recorded a flying bird in stiff headwind to increase the recording time. The system was calibrated with a camera pinhole model and lens distortions were corrected. Sparse correspondences were found with a correlation based method and a SIFT algorithm. The complexity was reduced by masking the falcon from the stationary background. The sparse point pairs allowed for usage of a Deep Flow Optical Flow algorithm. To increase the amount of correspondences a multi view method, the Trifocal tensor, was used. Most of the program allow for the parallelization on multiple workers to reduce the computational time. To obtain the 3D point cloud a optimal triangulation method is performed that minimizes the geometrical distance error. Finally the back projection error was measured and by means of a well-defined plate the uncertainty along the Z-axis was presented. Overall the method allows for the calculation of the wing surface of the bird over a time span. It has been shown that the resulting surface information can be used to analyze the aerodynamic properties like wing span, chord length, angle of attack and the variation over a flapping period without influencing the bird. This makes the qualitative aerodynamic analysis of the free flying birds possible and allows to deepen the locomotion of birds. The results show the high dynamic fluctuations of the aerodynamic properties during the flapping cycles. In addition, the analysis of a profile cross-section revealed a new perspective on what happens during up- and downstroke. Qualitative facts, such as the negative angle of attack at the stroke, made it possible to describe the complex movement of the falcon. The analysis shows the potential of the developed measuring system and the advantage of wind tunnel investigations for aerodynamic investigations of birds as other flying animals.

REFERENCES

[1] Thomas Bachmann and Hermann Wagner. The three-dimensional shape of serrations at barn owl wings: towards a typical natural serration as a role model for biomimetic applications. *Journal of Anatomy*, 219:192–202, 2011.

[2] Alexander Friedl and Christian J. Kähler. Measuring and Analyzing the Birds Flight. In *STAB Fach-Symposium zur Strömungsmechanik*, 2010.

[3] Thomas Wolf and Robert Konrath. Avian wing geometry and kinematics of a free-flying barn owl in flapping flight. *Experimental Fluids*, 56:1–23, 2015.

[4] Larry Li. Time-of-flight camera–an introduction. *Technical White Paper, May*, 2014.

[5] Benjamin Ponitz, Anke Schmitz, Dominik Fischer, Horst Bleckmann, and Christoph Brücker. Diving-flight aerodynamics of a peregrine falcon (falco peregrinus). *PLoS ONE*, 9(2):1–13, 02 2014.

[6] Anna C. Carruthers, Simon M. Walker, Adrian L.R. Thomas, and Graham K. Taylor. Aerodynamics of aerofoil sections measured on a free-flying bird. *Proceedings of the Institution of Mechanical Engineers, Part G: Journal of Aerospace Engineering*, 224(8):855–864, 2010.

[7] LaVision. Personal correspondence with employee. 2015. Munich.

[8] OpenCV. *OpenCV 2.4.9 documentation*, 2016.

[9] Andrea Fusiello, Emanuele Trucco, and Alessandro Verri. A compact algorithm for rectification of stereo pairs. *Machine Vision and Applications*, 12:16–22, 2000.

[10] OpenCV. *OpenCV 3.0 documentation*, 2017.

[11] Thomas Brox, Andres Bruhn, Nils Papenberg, and Joachim Weickert. High Accuracy Optical Flow Estimation Based on a Theory for Warping. *Lecture Notes in Computer Science*, 3024:25–36, 2004.

[12] Martin Heinold and Christian J. Kähler. *Image and Video Technology: 7th Pacific-Rim Symposium, PSIVT 2015, Auckland, New Zealand, November 25-27, 2015, Revised Selected Papers*, chapter Wing-Surface Reconstruction of a Lanner-Falcon in Free Flapping Flight with Multiple Cameras, pages 392–403. Springer International Publishing, Cham, 2016.

[13] Jianbo Shi and Carlo Tomasi. Good features to track. In *Computer Vision and Pattern Recognition, 1994. Proceedings CVPR'94., 1994 IEEE Computer Society Conference on*, pages 593–600. IEEE, 1994.

[14] John P. Lewis. Fast normalized cross-correlation. *Vision interface*, 10(1):120–123, 1995.

[15] Robert M. Haralick and Linda G. Shapiro. *Computer and Robot Vision*. Addison-Wesley Longman Publishing Co., Inc., Boston, MA, USA, 1st edition, 1992.

[16] David G. Lowe. Distinctive Image Features from Scale-Invariant Keypoints. *International Journal of Computer Vision*, 60(2):91–110, 2004.

[17] Relja Arandjelovic and Andrew Zisserman. Three Things Everyone Should Know to Improve Object Retrieval. In *Proceedings of the 2012 IEEE Conference*

on Computer Vision and Pattern Recognition (CVPR), CVPR '12, pages 2911–2918, Washington, DC, USA, 2012. IEEE Computer Society.

[18] Andrea Vedaldi. An open implementation of the SIFT detector and descriptor. Technical report, University of California at Los Angeles, 2007.

[19] Richard Hartley and Andrew Zisserman. *Multiple View Geometry in computer vision*. Cambridge University Press, second edition, 2004.

[20] Philippe Weinzaepfel, Jerome Revaud, Zaid Harchaoui, and Cordelia Schmid. Deepflow: Large displacement optical flow with deep matching, 2013.

[21] Michael Stoll, Sebastian Volz, and Andrés Bruhn. Adaptive Integration of Feature Matches into Variational Optical Flow Methods, 2013.

[22] Radu Bogdan Rusu, Zoltan Csaba Marton, Nico Blodow, Mihai Dolha, and Michael Beetz. Towards 3D point cloud based object maps for household environments. *Robotics and Autonomous Systems*, 56(11):927–941, 2008.

[23] Simon M. Walker, Adrian L.R. Thomas, and Graham K. Taylor. Photogrammetric reconstruction of high-resolution surface topographies and deformable wing kinematics of tethered locusts and free-flying hoverflies. *Journal of The Royal Society Interface*, 6(33):351–366, 2009.

[24] Werner Nachtigall. *Warum die Vögel fliegen*. Rasch und Röhring, 1985.

[25] Martin Heinold and Christian J. Kähler. Aerodynamic investigation of the free flapping flight of a saker falcon with the help of 3d multi-view reconstruction method. In *2018 Applied Aerodynamics Conference*, page 3173, 2018.

[26] Mark Drela and Harold Youngren. Xfoil 6.9. *User Guide. MIT*, 2001.

[27] Sebastian L. Herbst, Christian J. Kähler, and Rainer Hain. Sd7003 airfoil in large-scale free stream low-turbulence. In *47th AIAA Fluid Dyn. Conf.*, Denver, USA, 2017.

[28] Jan Van Ingen. The e^N method for transition prediction. Historical review of work at TU Delft. In *38th Fluid Dynamics Conference and Exhibit*, page 3830, 2008.

[29] Werner Reichardt. Verhaltensstudie der musterinduzierten Flugorientierung an der Fliege Musca domestica. In *Verhaltensstudie der musterinduzierten Flugorientierung an der Fliege Musca domestica. Biophysik des Tierflugs*, pages 7–72. Springer, 1974.

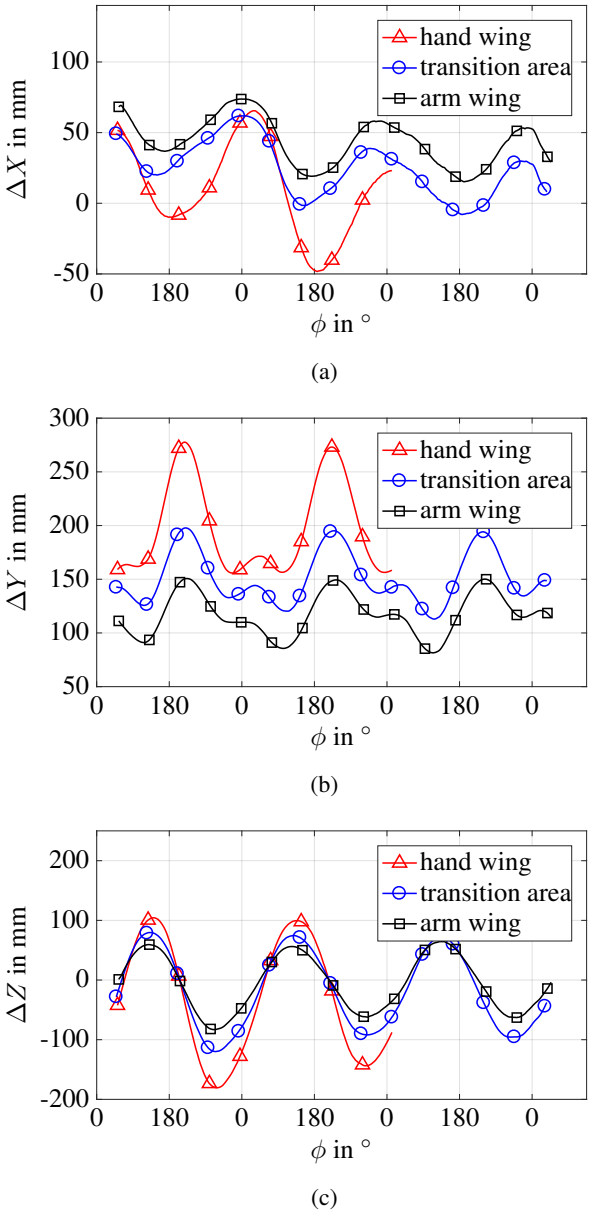

Figure 18: Distance of the three selected points on the wing to the point on the back of the bird displayed over the phase angle. Each plot shows a coordinate direction. (a): distance in X_b direction, (b): distance in Y_b direction, (c): distance in Z_b direction

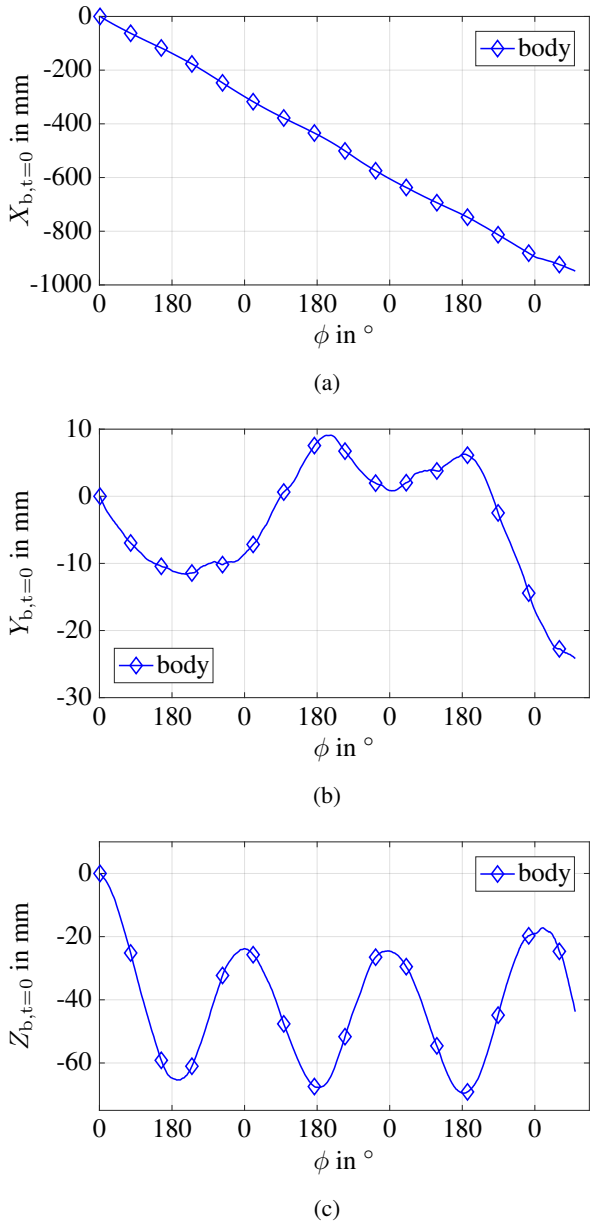

Figure 19: Movement of the body relative to a coordinate system on the back of the bird at the first time of evaluation t_0 applied over the phase angle. (a): motion in $X_{\mathrm{b,t=0}}$ direction, (b): motion in$Y_{\mathrm{b,t=0}}$ direction, (c): motion in $Z_{\mathrm{b,t=0}}$ direction

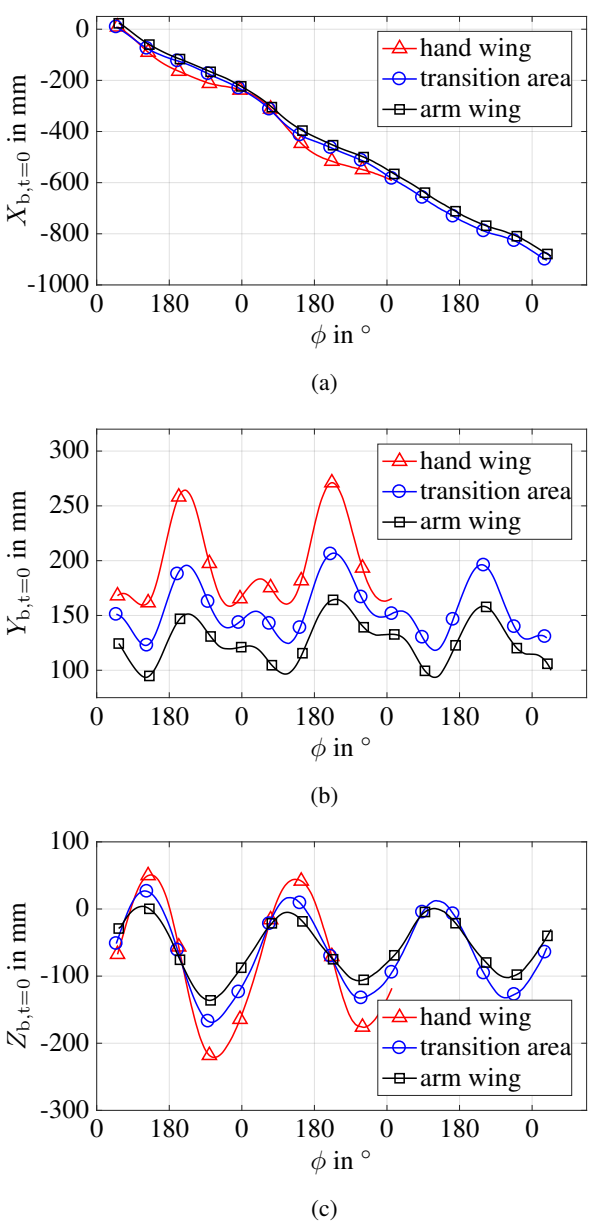

Figure 20: Movement of the Saker falcon wing relative to a coordinate system on the back of the bird at the first time of evaluation t_0 applied over the phase angle. (a): motion in $X_{\mathrm{b,t=0}}$ direction, (b): motion in$Y_{\mathrm{b,t=0}}$ direction, (c): motion in $Y_{\mathrm{b,t=0}} - Z_{\mathrm{b,t=0}}$ direction

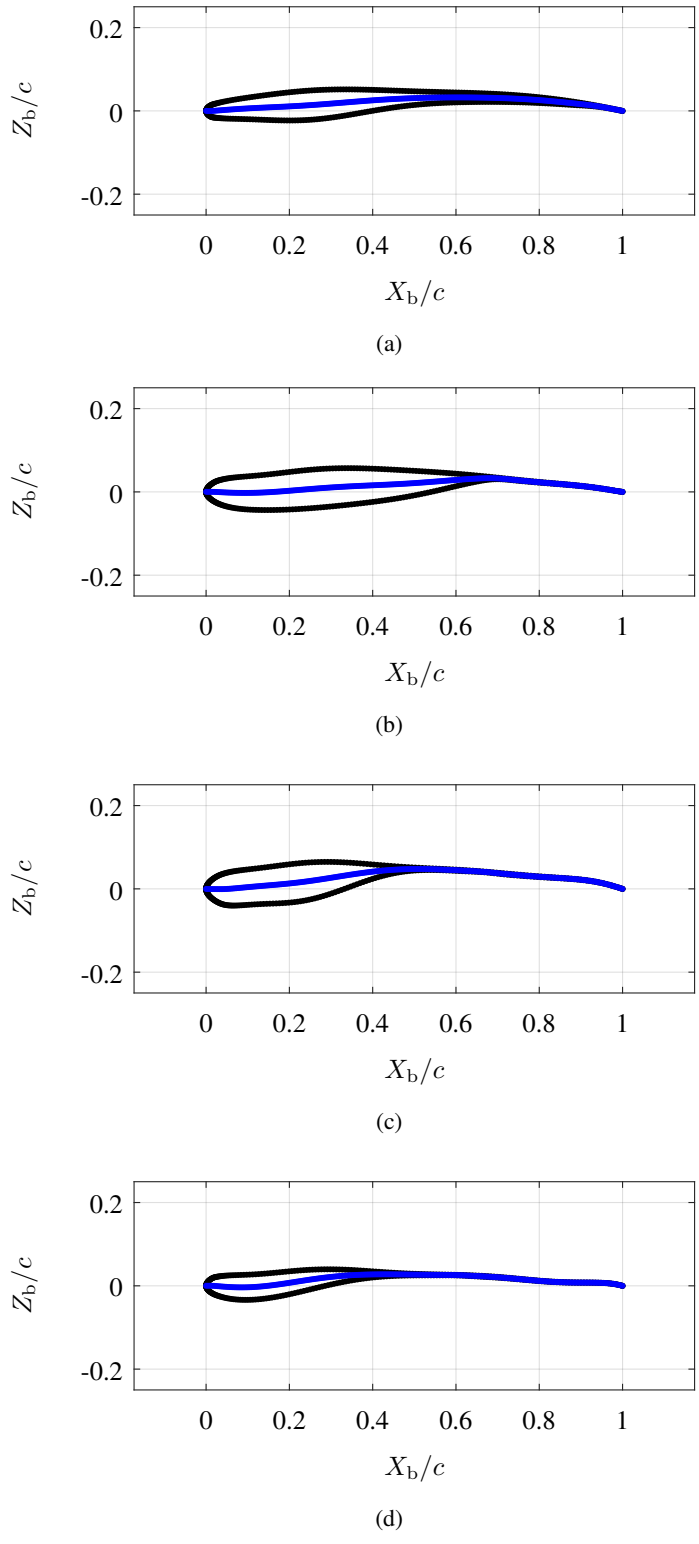

Figure 21: Wing cross section at $\zeta = 0.55$ on the right wing. $\Delta t = 25\,\mathrm{ms}$ between consecutive Figures.

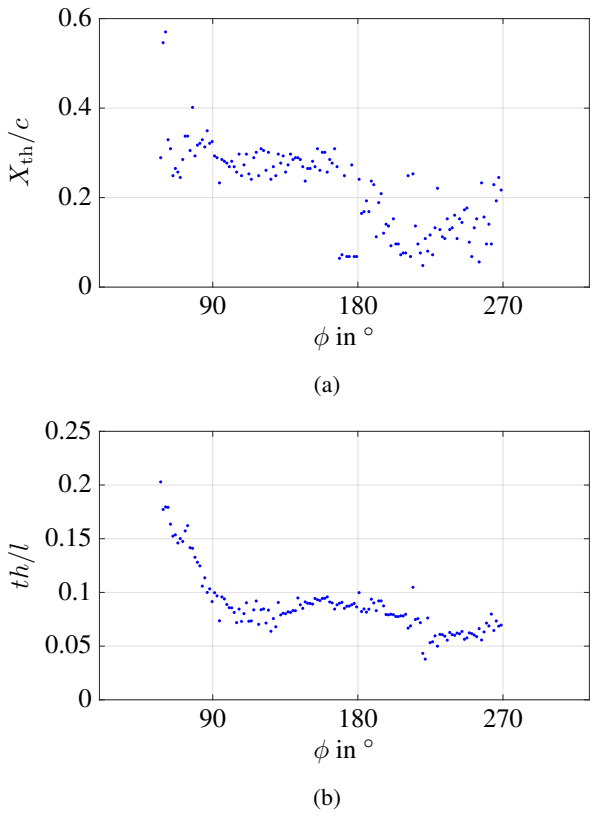

Figure 22: Distribution of maximum thickness values (th/c) and positions (X_{th}/c).

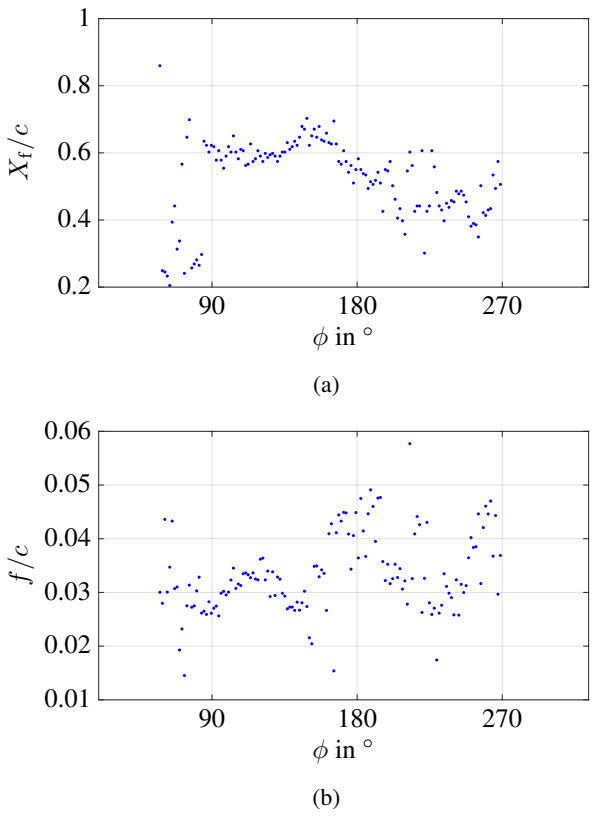

Figure 23: Distribution of maximum camber values (f/c) and positions (X_{f}/c).

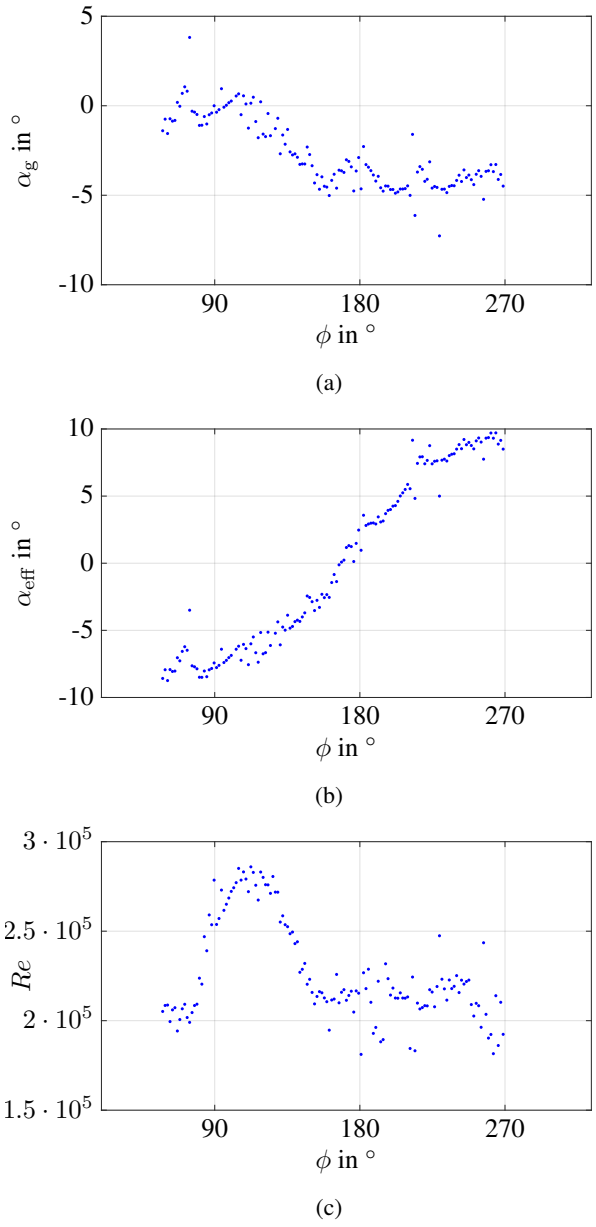

Figure 24: Angle of attack variation α_g and α_{eff} as well as variation of the Reynolds number Re over phase angle.

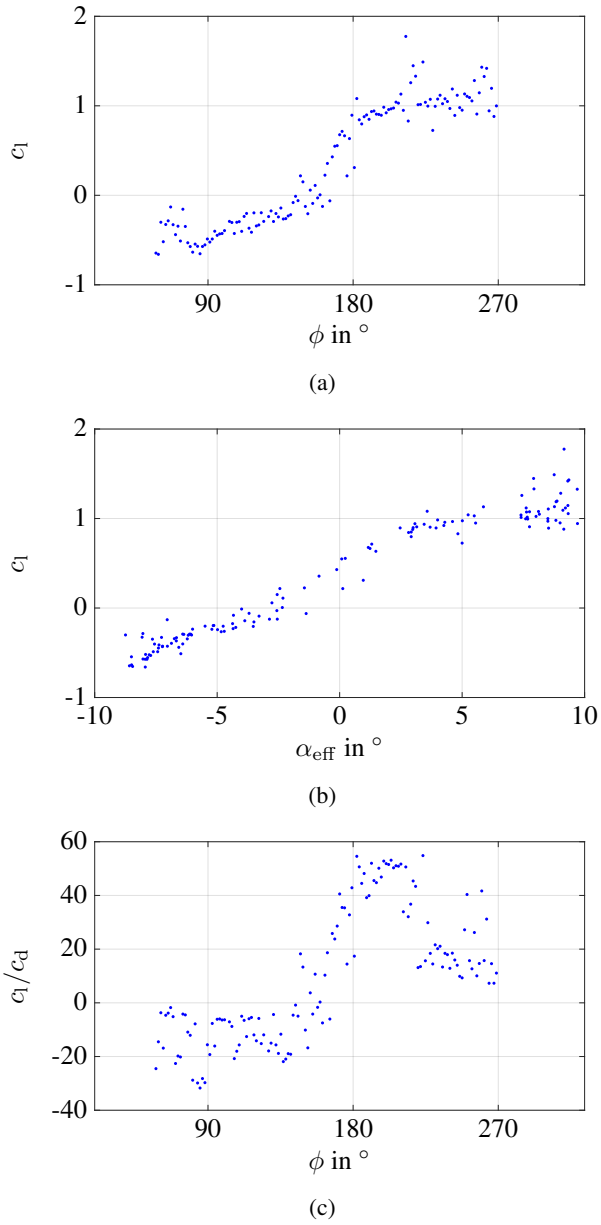

Figure 25: Lift coefficient over phase angle and different effective AOAs as well as lift-to-drag coefficient c_l/c_d over phase angle.